

Title	FIB patterning of stainless steel for the development of nano-structured stent surfaces for cardiovascular applications
Authors	Schmidt, Michael;Nazneen, F.;Galvin, Paul;Petkov, Nikolay;Holmes, Justin D.
Publication date	2013-12-06
Original Citation	SCHMIDT, M., NAZNEEN, F., GALVIN, P., PETKOV, N. & HOLMES, J. D. 2013. FIB Patterning of Stainless Steel for the Development of Nano-structured Stent Surfaces for Cardiovascular Applications. In: WANG, M. Z. (ed.) FIB Nanostructures. Cham: Springer International Publishing. http://dx.doi.org/10.1007/978-3-319-02874-3_16
Type of publication	Book chapter
Link to publisher's version	http://link.springer.com/chapter/10.1007/978-3-319-02874-3_16 - 10.1007/978-3-319-02874-3_16
Rights	© Springer International Publishing Switzerland, 2013. The final publication is available at Springer via http://dx.doi.org/10.1007/978-3-319-02874-3_16
Download date	2024-05-09 13:56:10
Item downloaded from	https://hdl.handle.net/10468/2468



UCC

University College Cork, Ireland
Coláiste na hOllscoile Corcaigh

16.2 Surface Treatments to Gain Desired Properties: Coating, Polishing, Patterning 46
47

There are various ways to improve the stent design in order to make it more effective. One way is coating the surface with organic and inorganic materials. This is not trivial with the complex geometry of the stainless steel mesh. Nevertheless this route is extensively studied given its benefit of incorporating drugs into the polymer-based surface coating which can be eluted over time into the surrounding vessel material. However, there are several reasons, including concerns about increased risks of late stent thrombosis when using drug-eluting stents [8, 9], why the development focus is likely to return to bare metal or polymer-free stent technologies [3].

While from the invention of stents it was aimed for a surface as smooth and polished as possible in order to minimise abrasion and inflammation of the body tubes, it becomes ever more apparent that a somewhat roughened/textured surface might be a better fit for the task.

16.3 Biomaterial–Cell Interaction: Advantages of Rough/Patterned Surfaces 60
61

The influence of textured material surfaces on the behaviour of cells has been studied for many years by now [10–16]. On one hand, theoretical studies show that cells prefer to grow on rough surfaces in general as it imitates best naturally occurring surfaces [17]. On the other hand, in order to have a better control over and to minimise the complexity of the experimental conditions, the natural urge to study regular patterns led scientists from rough to micro- to nano-patterned surfaces. Especially in tissue engineering where the tissues involved require certain mechanical and structural properties for proper functioning, the trend from micro- to nano-structured surfaces serving as artificially created support systems has become evident within the last decade [18–24]. Also for drug delivery the control over biointerfacial interactions is often the key to biomedical applications [14].

In particular endothelial, smooth muscle and fibroblast cells play an important role in the healing process and maintenance of cardiovascular systems and thus are likely to be in contact with biomedical implants such as stents and grafts. During a surgical procedure involving the introduction of a stent, vascular tissues in the arteries may be damaged. Healing of vascular tissues is promoted by the formation of an endothelial cells lining on the stent substrate [25], while the presence of smooth muscle cells and fibroblasts may cause re-stenosis. Micro- and nano-textures on substrates may provide control of cell functions. Such structures could promote better vascular cell adhesion, decrease the need for systemic administration of drugs and reduce the requirement for secondary surgery after stent implantation.

83 16.4 Patterning: Lithography, Electrodeposition, Dip Pen, 84 Pulsed Laser, FIB

85 Recent advances in micro- and nanotechnology have allowed the patterning of sur-
86 faces with the desired textures for cell scaffolding [26–29]. Nano-texturing involves
87 the creation of patterns or features with nanometre precision. The choice of the
88 texturing method depends largely on the nature of the substrate that needs to be
89 modified and on the dimensions of the features expected. Indeed, photolithography
90 was particularly successful for the patterning of features of microscopic dimensions
91 on elastomers such as polydimethylsiloxane (PDMS) [30–33] and on polymers such
92 as polystyrene (PS) [34–37]. E-beam lithography was used for the patterning of
93 submicron features on silicon substrates [38, 39] and on poly(methyl methacrylate)
94 (PMMA) [40]. Features of 350 nm were patterned on PDMS and PMMA substrates
95 by nanoimprint lithography [41]. Metal substrates such as Ti were also textured
96 using micro-machining for feature dimensions in the microscopic range [10, 42].
97 Cell adhesion, migration, elongation, proliferation and gene expression on textured
98 substrate can be greatly altered depending on the shape and the dimension of the
99 features [40].

100 The different techniques are compared in Table 16.1. In indirect photolithogra-
101 phy methods, patterns are formed over a large area using a mask [43]. Such lithog-
102 raphy processes are time consuming with many steps and inherently inappropriate
103 for prototype designs and processes. Electrodeposition is a simple, fast and cost-
104 effective method of reproducing nano-structures on many materials using templates
105 made of polymers and metals. However, this method is applicable only for electri-
106 cally conductive substrates. Imprint lithography is a high-resolution direct tech-
107 nique for nano-patterning of large surfaces, but it requires moulds and is restricted
108 to polymeric materials [44], but this could then be used as etch masks or filled with
109 metal electrodeposition. E-beam lithography and lithography based on scanning
110 tunnel microscopy (STM), atomic force microscopy (AFM) or dip pen are high-
111 resolution mask-less procedures, but with a very low throughput and unsuitable for
112 wide surface nano-patterning [45]. Interference lithography can be utilised to create
113 or transfer array patterns on various metallic and polymeric surfaces, but only pat-
114 terned features can be reproduced. Microtexturing of surfaces has also been reported
115 by pulsed laser patterning [46, 47]. The feature sizes are however limited to the
116 micron range.

117 Patterning by FIB milling is direct and offers several advantages for flexible
118 prototyping: (1) practically any substrate material that is able to withstand high
119 vacuum conditions of the microscope chamber can be used, (2) there is high flexi-
120 bility in the obtainable shapes and geometries by modulating the ion beam current
121 and the patterning conditions, (3) reduced complexity of the patterning process, e.g.
122 it is a single-step process with a possibility of real-time monitoring of the milling
123 progression. Thus for any particulate type of substrate, various depths as well as
124 lateral dimensions including the optimal feature size can be obtained at minimum
125 number of processing steps.

t1.1 **Table 16.1** Advantages and disadvantages of indirect and direct nano-structuring techniques

t1.2	Mask/ t1.3 moulds t1.4 required	Nano-fabrication t1.4 techniques	Advantages	Drawbacks
t1.5	Yes	Photolithography	Well-controlled features	Requires photoresist, spin coaters and organic solvents
t1.6			High throughput	Low aspect ratio
t1.7		Electrodeposition	Precise geometries and patterns	Limited to set of materials
t1.8			Large surface area	Require templates for creating of nano-structures
t1.9				Limited to electrically conducting substrates
t1.10		Imprint lithography	High resolution	Requires moulds
t1.11			High aspect ratio	Applied to polymers only
t1.12			Large surface	
t1.13	No	E-beam	High resolution	No direct writing on substrate
t1.14			Precise geometry and patterns	Multistep process
t1.15				Low throughput
t1.16				Requires vacuum
t1.17				Time consuming
t1.18				Small surface coverage
t1.19				Expensive
t1.20		Interference lithography	No complex optical systems	Limited to patterned array features only
t1.21				Multistep process
t1.22		STM/AFM/dip pen	Very high resolution	Low aspect ratio
t1.23				Very low throughput
t1.24				Very small surface area
t1.25		Nanoindentation	High aspect ratio	Wide and shallow features
t1.26			Control over features depth	Slow process
t1.27			Less expensive than FIB or e-beam writer	
t1.28		Laser patterning	Any material	Wide and shallow features
t1.29			High throughput with high power laser	Micron resolution
t1.30		FIB milling	High resolution	Time consuming
t1.31			High aspect ratio	Process requires vacuum
t1.32			High etch rate	Very expensive
t1.33			Any material	Low throughput

16.5 FIB Advantages: Fast for Prototyping

126

Except FIB, none of the texturing techniques mentioned above were suitable to achieve features in the nanoscopic range on a hard substrate as 316L stainless steel. Nanoimprint lithography (NIL) and e-beam lithography (EBL) are able to pattern submicron features, which with NIL were achieved on soft substrates such as polymers and elastomers only and with EBL is a very time-consuming and expensive multistep process. In this research work, FIB milling was used to create

127
128
129
130
131
132

133 nano-structures onto stainless steel because it is a direct writing process with simple
 134 steps, high resolution and aspect ratios. Nano-structured features such as pits were
 135 created on 316L steel surfaces. The optimal FIB patterning conditions for achieving
 136 reasonably high throughput (patterned rate of about 0.03 mm²/h) and nano-size
 137 accuracy in dimensions and shapes of the features are discussed. Additionally, a
 138 characterisation protocol for analysis of such structures by combination of electron
 139 backscattering diffraction (EBSD), FIB, scanning electron microscopy (SEM),
 140 atomic force microscopy (AFM) and serial FIB–SEM sectioning is detailed.
 141 Furthermore, this chapter reports the comparison of in vitro EC adhesion and growth
 142 on FIB nano-structured, unpolished and electropolished 316L steel surfaces.

143 16.6 FIB Overview: Ga⁺ Beam, Maskless, Pattern Design

144 FIB systems usually employ a finely focused beam of gallium ions (Ga⁺) that can be
 145 operated at high beam currents for milling or low beam currents for imaging. It can
 146 be utilised to remove material locally in a highly controlled manner to the nanome-
 147 tre scale. When the high-energy Ga ions impinge the sample, atoms from the sample
 148 surface are sputtered. In addition, Ga atoms from the ion beam are also implanted
 149 into the top few nanometres of the surface, and the surface is made amorphous. As
 150 can be seen in Fig. 16.2, the Ga⁺ primary ion beam hits the sample surface and sput-
 151 ters a small amount of material. The primary beam also generates secondary elec-
 152 trons. When the primary beam strikes the sample surface, the signal from secondary
 153 electrons or sputtered ions is collected to form an image of the surface [48].

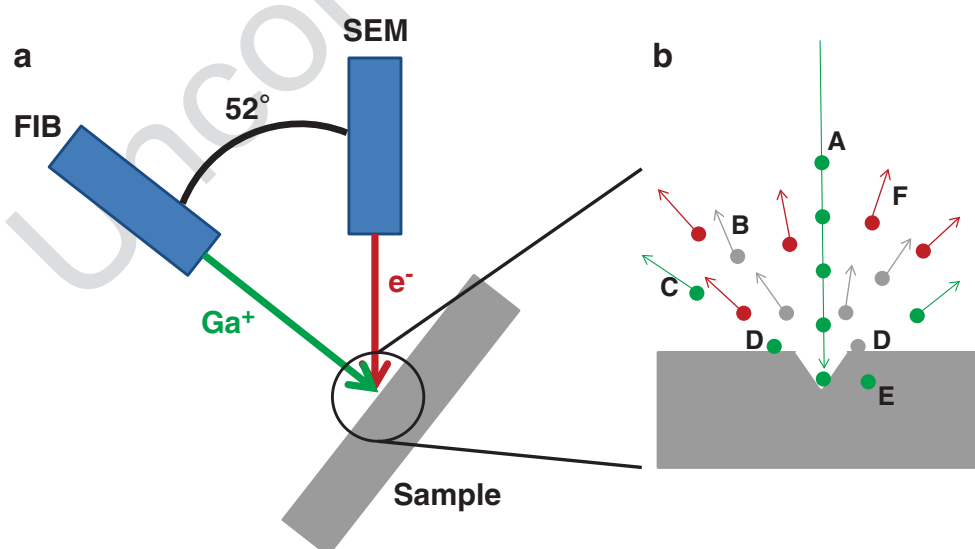


Fig. 16.2 (a) Dual-beam FIB schematics. (b) Beam sample interactions: *A*—incident Ga⁺ ions, *B*—sputtered substrate atoms, *C*—scattered Ga⁺ ions, *D*—re-deposited Ga⁺ ions and substrate atoms, *E*—in substrate trapped Ga⁺ ions and *F*—secondary electrons

At a low primary ion beam current, a minuscule amount of material is sputtered, and with existing FIB methods, 5 nm resolution can be attained using Ga ions. However, at higher primary ion beam current, a considerable quantity of material can be taken out, which allows sub-micrometre- to nanometre-scale precision milling of sample surface.

FIB originated in the semiconductor industry and has become an important tool for a wide array of applications, ranging from circuit editing, reverse engineering, sample preparation for transmission electron microscopy (TEM), microstructural analysis and prototype nanomachining to name just a few [49]. Many modern FIB instruments supplement the FIB column with an additional SEM column so that it becomes a versatile dual-beam platform as depicted in Fig. 16.2. In nano-patterning, FIB has been used to create nano-structures on Si [50], silicon nitride [48, 51] and glass substrates [52] and to fabricate platinum nano-structures on peptide-based soft surfaces [53]. Only one study reported the protein adsorption on FIB patterned glass surfaces [52]. To date, no cellular studies have been reported on FIB-structured surfaces. Moreover, this and other aforementioned techniques have not been employed for patterning the key vascular stent material 316L stainless steel for vascular cell functions. Studies do not exist that determine the EC response on 316L steel with nano-pit features. Endothelial cell studies on unpatterned 316L stainless steel substrates have shown that the grain size and grain boundaries have an impact on their adhesion and morphology [54]. Chemically etched substrates with 16 µm grain size etched have demonstrated cell densities significantly higher than with grain sizes of 31, 47 and 66 µm. The authors attribute this increased cell density to greater boundary area and associated higher surface free energy [54]. Cell proliferation was also subject to another study discussing different materials. There the grain sizes varied from 320 nm to 22 µm. Again cell proliferation was reciprocal dependent on the grain size [55].

16.7 Crystal Structure of Stainless Steel 316L

Austenitic type 316L stainless steel is commonly used for manufacturing medical implants [56] and was hence selected as the substrate of choice for this study. Austenitic stainless steels have face-centred cubic (fcc) crystal structure, in which the unit cell is a cube with atoms located at the corners and middle of each side (Fig. 16.3a). The presence of higher concentration of Ni in austenitic stainless steels stabilises the fcc crystal structure, because Ni is a fcc crystal itself. This enhances the ductility, i.e. it can sustain large plastic deformation without fracture compared to other stainless steels (martensitic and ferritic phases).

[AU2]

Most metallic materials are composed of many small single-crystalline planes called grains. These materials are referred to as polycrystalline materials (e.g. steel), in which individual grains have identical arrangement of atoms but the orientation of the atom arrangement or crystal structure is different from each adjoining grain (see Fig. 16.3b for visualisation). The interfaces between these grains are grain boundaries, the surface that separates the individual grains [57].

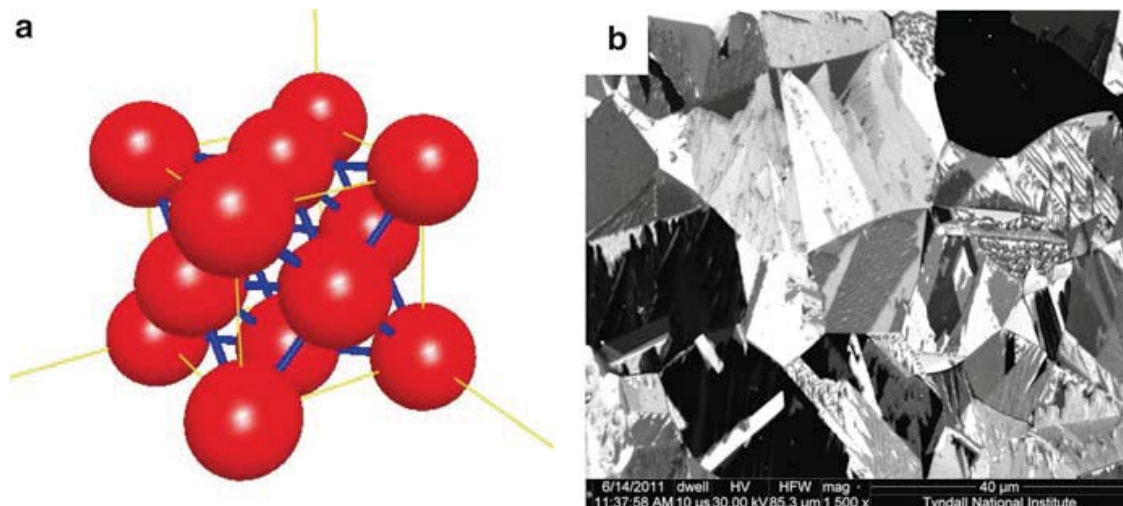


Fig. 16.3 (a) Schematic face-centred cubic crystal structure and (b) FIB image of polycrystalline 316L used in this study

195 The austenitic stainless steel function can be affected by two microstructure fea-
196 tures: grain (or crystal) size and shape. The general grain size suggested for 316L is
197 100 μm or less [56]. This is because smaller grains have more grain boundaries,
198 which provide resistance to plastic deformation as they are responsible for slip
199 deformation by dislocations.

200 Depending on the process conditions such as annealing and cold-working, the
201 shape of austenitic stainless steel grains varies. Annealing is a heat treatment process
202 where a material is modified, resulting in changes in its properties, for example,
203 strength and hardness. It is a method that generates conditions via heating to above
204 the recrystallisation temperature, maintaining an appropriate temperature, and subse-
205 quently cooling. This method is applied to reduce internal tensions, soften material,
206 enhance ductility, improve the structure by creating it uniform and enrich cold-work-
207 ing properties. Austenite grains of the stainless steels under an annealed condition
208 exhibit an equiaxial granular shape (i.e. the grains having axes of equal length).

209 Cold-working produces plastic deformation in the steels and generates a strain
210 hardening effect, which improves both yield strength and tensile strength of steel
211 considerably. However, in cold-worked steel, depending on the amount of cold work,
212 the grains are elongated (i.e. longer in the rolling direction). During large plastic
213 deformation, textured grain structures are produced and preferentially align the grains
214 in specific crystallographic orientations. Hence, cold-worked steel with textured
215 structures demonstrates anisotropic mechanical properties. When employing a cold-
216 worked steel for implant fabrication, microstructure analysis is suggested as implants
217 can be better prepared if the loading direction is concurrent to the high strength direc-
218 tion in the steel [56]. Hence, it is clear that the microscopic and crystalline structure
219 can play a strong role on the nano-structuring of the stainless steel surface.

[AU3]

16.8 Substrate Preparation: Electropolishing, Cleaning

220

Electropolished 316L steel substrates were used for this study. Figure 16.4 illustrates the steps involved in the whole sample process flow. Electropolishing of steel was performed with a view to the preparation of these surfaces for nano-texturing. For such applications, a smooth surface is crucial. The composition of this electrolyte solution was 11 M H_3PO_4 + 4.5 M H_2SO_4 in water. The electropolishing procedure was conducted in two steps at 80 °C and 5 mV s⁻¹ [58]. The first step involved scanning of the potential from the open-circuit potential up to the point where the diffusion-limited current region was reached. The linear sweep voltammetry was then stopped, and the selected potential was maintained 10 min using chronoamperometry. This resulted in a smooth and relatively defect-free surface. XPS analysis of the electropolished surface has shown that the stainless steel was enriched with Cr, P, S, O, Mo and Ni elements. Prior to nano-structuring, the polished specimens were cleaned in acetone, in ethanol and finally in ultrapure water via an ultrasonic treatment for 10 min.

16.9 FIB Tests: Challenges with Anisotropic Milling

235

The FIB system used in the current study is the FEI Helios NanoLab 600i, which is a dual-beam FIB for localised milling and deposition, transmitting a 30 keV beam of Ga⁺ ions combined with a high-resolution SEM. In this work, the working current was tuned between 0.28 nA (for 120 nm pits) and 0.92 nA (180 nm) depending on size of the nano-texture. The available pit sizes and the large range of obtainable working currents could make the FIB technique an ideal device for nanomachining in the range from 10 nm to a few micrometres. Nano-structured features (pits/holes) ordered in rectangular arrays were patterned on 316L steel surfaces using FEI Helios NanoLab 600i FIB system. This system was used because of high beam quality and stage stability.

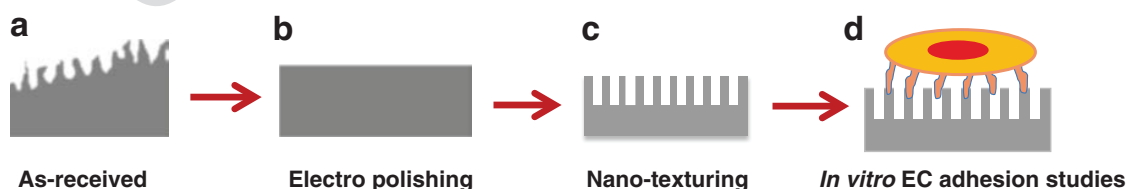


Fig. 16.4 Sample process flow in total. (a) Samples as received with rough surface. (b) Electropolishing to obtain a smooth surface suitable for nano-structuring. (c) Nano-texturing of 316L stainless steel via a focussed ion beam (FIB) milling. (d) In vitro endothelial cell adhesion studies

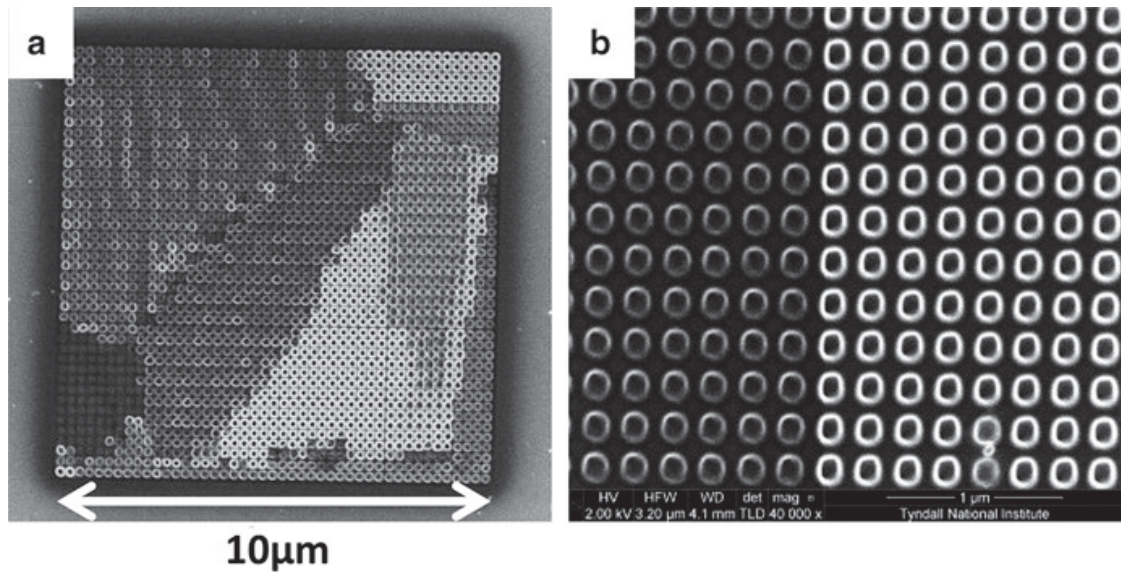


Fig. 16.5 SEM images of preliminary FIB tests to determine the feasibility of the prototyping approach. (a) $10 \times 10 \mu\text{m}$ area pattern by FIB in preliminary tests with nominal 120 nm wide pits at 240 nm pitch. (b) Detail of another area exhibiting the same pattern. Clearly visible are the differences in appearance of the patterned surface depending on the polycrystallinity of stainless steel

246 From the literature survey, promising cell responses to nano-structured features
 247 were identified including nano-pit features [40, 59]. However, to date no EC studies
 248 have been reported on nano-pit structures. Based on this, two pit designs were pat-
 249 terned on three electropolished 316L stainless steel samples on areas of
 250 $400 \mu\text{m} \times 400 \mu\text{m}$ using FIB: design A, pits of 120 nm diameter with a pitch of
 251 240 nm and intended depth of 50–100 nm, and design B, pits of 180 nm diameters
 252 with pitch of 360 nm and intended depths of 50–100 nm [60, 61].

253 Before attempting prototyping on large $400 \times 400 \mu\text{m}$ areas used for the biologi-
 254 cal tests, we have performed optimisation tests on relatively small test patterns; one
 255 such area is shown in Fig. 16.5a. From the known polycrystalline nature of the 316L
 256 stent material, one can assume that when subjected to ion milling or imaging, it will
 257 show pronounced channelling contrast. It is well known for about a century for W,
 258 Ag or Cu which are all fcc metals that they etch and sputter faster in preferred direc-
 259 tions [62–65], as well as Si [66, 67]. Similarly polycrystalline fcc austenitic stain-
 260 less steel will show milling rates that are varying by the different orientation of
 261 grains towards the incoming beam.

262 Figure 16.5 illustrates how much this anisotropic milling affects the desired out-
 263 come of uniform concaves. Shown in Fig. 16.5 are examples from the pretests on
 264 $10 \mu\text{m} \times 10 \mu\text{m}$ areas with 120 nm diameter holes at 240 nm pitch. The structures
 265 that appear with the brightest contrast showed deeper and sharper edges than the
 266 structures that appear darker in contrast. This will be discussed in more detail in the
 267 following section describing the correlative microscopy approach. A later section
 268 will focus on the study on the patterned substrates used for actual cell adhesion tests
 269 and the preliminary FIB tests.

16.10 Correlative Microscopy: EBSD, FIB, SEM, AFM, and Serial Sectioning FIB–SEM Towards Better Understanding of Beam–Substrate Interaction 270
271
272

In order to gain a better understanding of the beam–substrate interaction during patterning, a correlative microscopy approach was used to illuminate the patterning process from many possible angles [68, 69]. This was also done on a batch of samples that could not be used for the cell adhesion studies basically because of the destructive nature of the last step, the serial FIB–SEM sectioning. 273
274
275
276
277

The different techniques used for the characterisation of nano-textured, unpolished and electropolished stainless steel surfaces were electron backscattering diffraction (EBSD), FIB, SEM, atomic force microscopy (AFM) and serial FIB–SEM sectioning. Figure 16.6 shows the detailed process flow of the correlative approach. 278
279
280
281

EBSD technique was used to analyse the crystallographic structured surfaces of the polished stainless steel. EBSD imaging was performed in a Hitachi SEM SU-70 equipped with an Oxford Instruments EBSD attachment AztecHKL at 10 kV under 70° tilt angle and step size 2 μm. 282
283
284
285

FIB technique was also used to visualise the crystallographic structured surfaces of the polished stainless steel. FIB imaging was performed as a part of monitoring of the milling at 30 kV accelerating voltage. 286
287
288

SEM was used to analyse the topography of nano-textured surfaces of the polished stainless steel. The SEM images presented were obtained using a SEM at the FEI Helios NanoLab 600i at an electron beam current of 5 kV and 86 pA beam current. 289
290
291

A commercial atomic force microscope (MFP 3DTM, Asylum Research) in AC mode was used for topography mapping of the films. Olympus AC160TS silicon cantilevers (Al reflex coated, ~300 kHz resonant frequency) were used for imaging. Optimal results were achieved with a medium scan rate of 1 Hz and 256 × 256 pixels image resolution. 292
293
294
295
296

Samples for serial sectioning were prepared using protective carbon and Pt layers [70]. The electron beam-induced (EBID) carbon deposition supplied necessary contrast difference between the protective Pt and the stainless steel surface, hence enabling accurate determination of the concave's shape and depth. 297
298
299
300

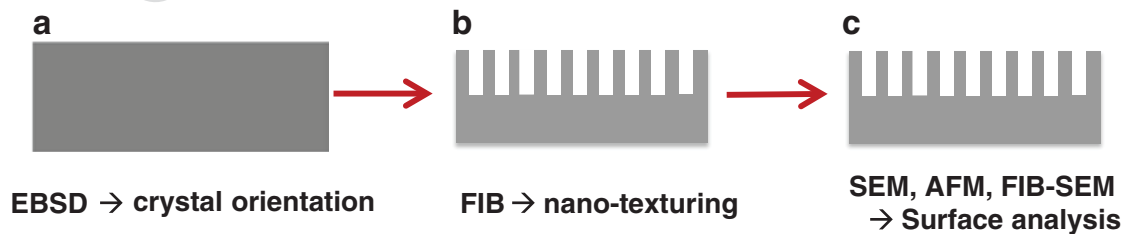


Fig. 16.6 Process flow in the correlative microscopy approach. (a) The crystallographic grain orientations are measured by EBSD before patterning. (b) Surface patterning using FIB, also gaining FIB SE images as part of the monitoring process. (c) Extensive analysis of the textured steel surface with SEM, AFM and finally destructive serial FIB–SEM sectioning

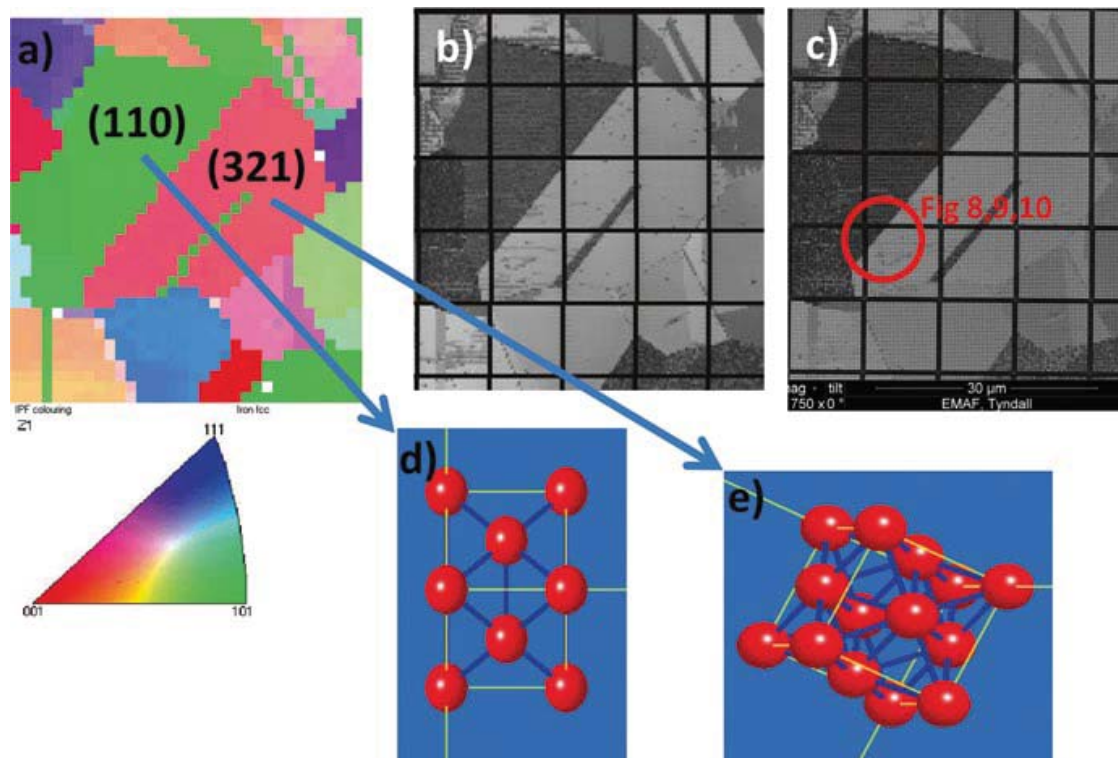


Fig. 16.7 Correlative microscopy on the exact same sample location. (a) Inverse pole figure (IPF) as measured by EBSD before surface texturing with (110) and (321) crystal orientation labelled and legend underneath. (b) FIB SE image obtained during patterning as part of monitoring. (c) SE image taken after the patterning—the red circle indicates the region used for AFM and serial sectioning (see Figs. 16.8, 16.9 and 16.10 for details). (d) Graphical visualisation of (110) orientation. (e) Graphical visualisation of (321) orientation

301 EBSD is an SEM-based microstructural–crystallographic technique to measure
 302 individual grain orientations, local texture, point-to-point orientation correlations
 303 and phase identification and distributions on the surfaces of bulk polycrystals. It is
 304 also known as backscatter Kikuchi diffraction (BKD), and both acronyms are being
 305 used interchangeably in the literature. EBSD patterns are generated on a phosphor
 306 screen by backscatter diffraction of a stationary beam of high-energy electrons from
 307 the typically 70° tilted sample surface. Because of the high tilt angle—or the shallow
 308 20° angle of the incident beam towards the surface—this technique is very surface
 309 sensitive and gives information of the top 20 nm down into the substrate [71].

310 EBSD mapping was accomplished before the area was patterned in order to
 311 determine a correlation between crystal grain orientation on one hand and shape,
 312 size and depth of the FIB-milled concaves on the other hand. Figure 16.7 shows the
 313 random size and orientation of the crystal grains and illustrates the correlative
 314 microscopy approach of three techniques combined in the exact same sample loca-
 315 tion, EBSD, FIB and SEM. In general the intensity of the emitted SE depends on the
 316 different inclination of the sample surface towards the incoming beam and crystal
 317 orientation [72]. Thus, the grey levels in the SEM image are directly linked to the

surface topography, e.g. the shape of the pits and sidewall profile and the crystal orientation of the surface material. In this way we can correlate the EBSD data to the grey levels in the SEM images. The FIB reveals not surprisingly the same contrast in the SE image as the one taken afterwards in the SEM. The SE yield is independent of the type of the beam; hence the same contrast is achieved. The additional information of the SEM SE image lies in the much higher resolution. The FIB which was run as a monitoring tool only during the patterning process produced one pixel every 360 nm in *X* and *Y* direction. The SEM on the other hand was used afterwards as an analysis tool with an image resolution of $4,096 \times 3,775$ pixels which calculates at roughly 3 nm image resolution. Using a low current of 86 pA ensured that the real resolution is not far from this theoretical limit.

Two different grains were chosen for additional correlation with AFM and the serial FIB–SEM sectioning based on the crystallographic orientation, a low index grain with (110) orientation and a high index grain with (321) orientation. From as early as the 1920s, it is known that the sputter yield is dependent on the crystal orientation [62]. It is also known that the SE yield is dependent on the crystal orientation [72]. Based on this fact the chosen grains should display a very different behaviour when exposed to the ion beam during sputtering and also to the electron beam in the SEM study.

Studying the marked region from Fig. 16.7 across the grain boundary using the AFM (see Fig. 16.8), it appears that there is a difference in hole depth and diameter depending on crystallographic orientation of the patterned surface. Even the shape of the rim is evidently not circular but rather rhombohedral. Because of the high aspect ratio of the pits, the tip could not reach down and probe the full depth of the pits; therefore, the pit depth must be confirmed by the serial sectioning.

The first that comes to mind when seeing the rhombohedral shape of the pits is the directional dependence in which atoms are ejected when sputtering at threshold energy [63]. In our study however the energy used to create the patterned surfaces in the FIB was way beyond the threshold energy, which for Cr, Ni and Fe as main elements in 316L lie in the range of 60–90 eV. The directional dependence decreases with higher sputter energies and has no influence on the direction of the sputtered atoms at the 30 keV used here. It is also obvious when looking in detail at the (111) oriented grain at the bottom of the AFM overview scan that shows the same rhombohedral-shaped pits as the whole area around this region instead of the expected triangular shape. As can be seen below in the detailed AFM and SEM studies on the $400 \mu\text{m} \times 400 \mu\text{m}$ patterns used for the cell adhesion studies, the shape of the holes is solely determined by the ion beam quality (focus, stigmation) at the place of impact on the sample surface.

In the SEM surface study as depicted in Fig. 16.9a, it appears as if the holes in both grains seem equal in diameter with only the higher SE yield obvious for the higher index grain. In order to clarify this impression, the region was imaged again after depositing a carbon layer as shown in Fig. 16.9b. Because secondary electrons are emitted from an area very close to the surface of the sample, this amorphous carbon layer masks the crystal orientation of the sample surface, and the image is

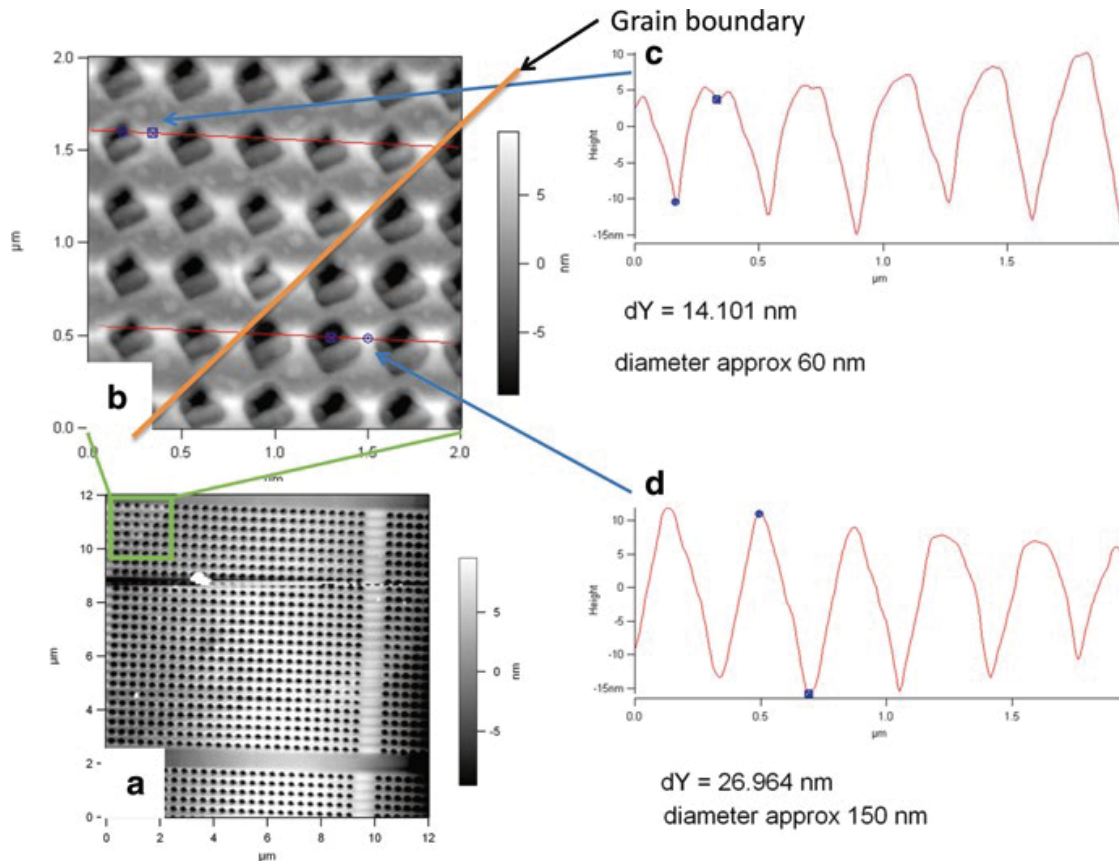


Fig. 16.8 Representative AFM scans of the marked region from Fig. 16.7. (a) Overview scan over the whole $12 \mu\text{m} \times 12 \mu\text{m}$ region. (b) Detailed $2 \mu\text{m} \times 2 \mu\text{m}$ scan of the area around the crystal grain boundary. (c) Line profile along one row of five holes determining depth and diameter of the holes in the (110) oriented grain. (d) Same line profile determining the depth and diameter of the holes in the (321) oriented grain

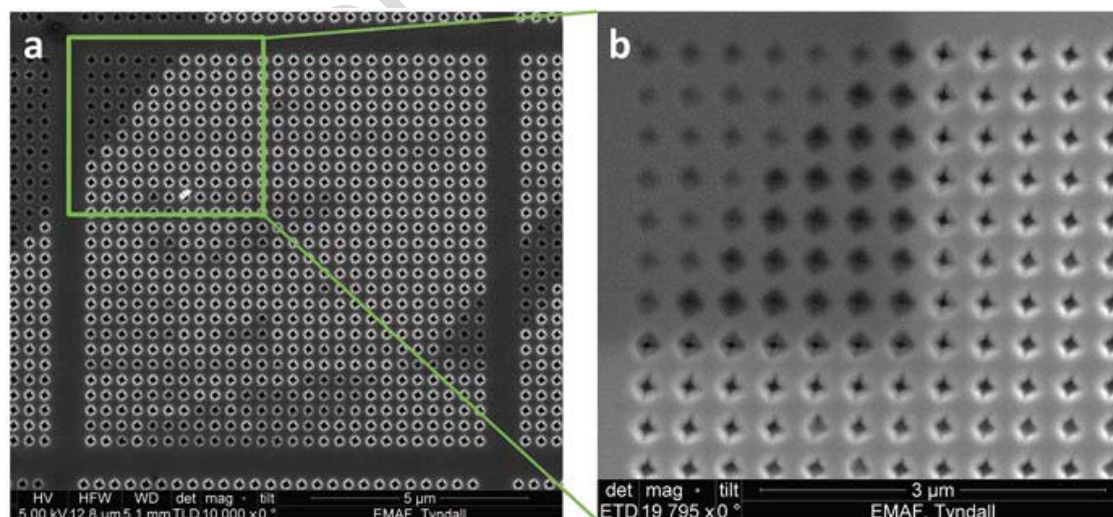


Fig. 16.9 Detailed SEM images of patterned area marked by the *red circle* in previous picture. (a) Freshly patterned surface displays high SE yield for the high index grain and low yield for the low index grain, though the holes seem equal in diameter. (b) Detail of (a) after carbon deposition, the “true” diameter shines through as crystal orientations are hidden behind the amorphous carbon layer

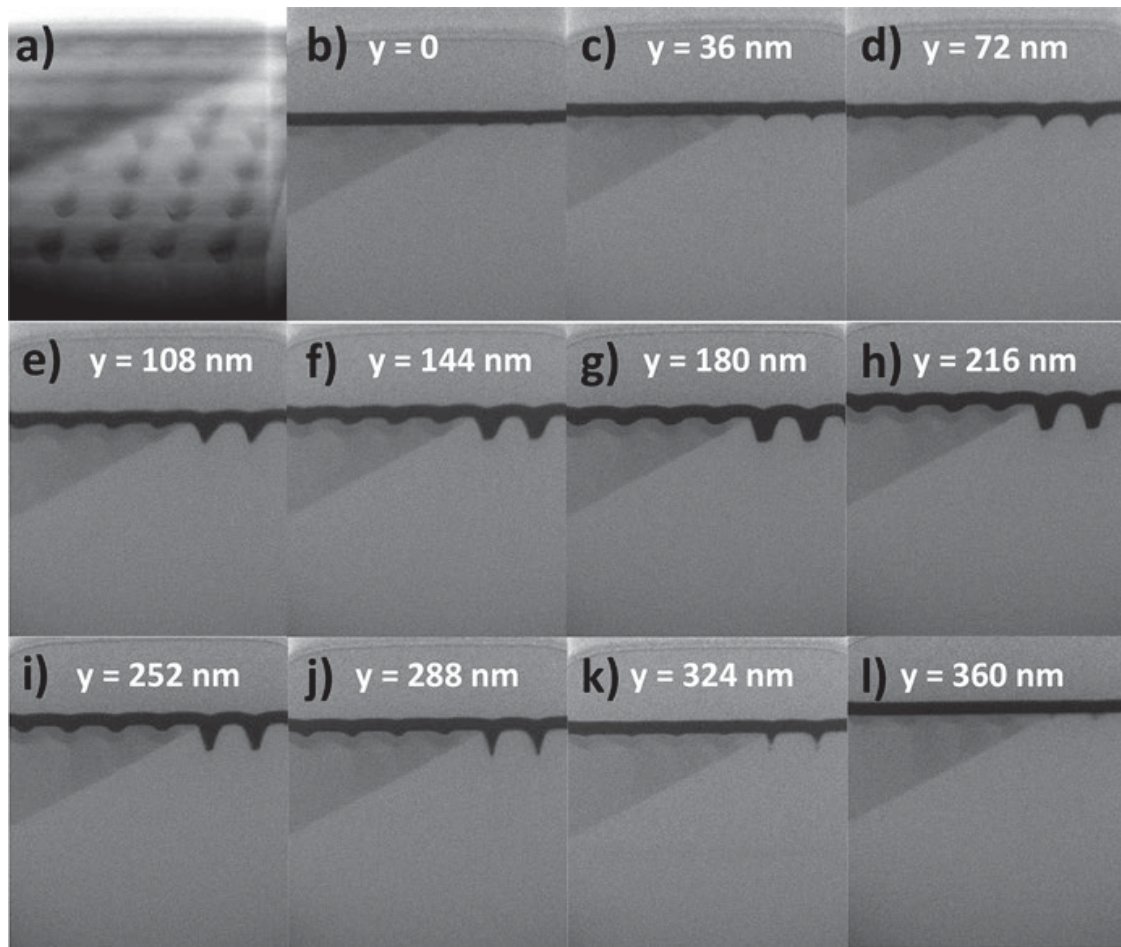


Fig. 16.10 Serial sectioning as final destructive step of the correlative microscopy. (a) 3D reconstruction of all the 250 slices. (b–l) Image series illustrating one row of six holes taken every 36 nm (every third image). The *darker left* region is the low index grain (110) oriented, the *brighter right hand side* is the higher index (321) oriented grain. Obvious is the difference in depth by more than a factor of 3 between the two patterned grains

more related to topographical features. Indeed, the difference in diameter of the 362
 holes becomes pronounced, and it is visible that the higher index grain has appar- 363
 ently much larger holes than the lower index grain. 364

Serial sectioning of again the same region was performed composing 250 images 365
 of 8 rows by 5 holes, with one image taken every 12 nm. This detailed analysis veri- 366
 fies the difference not only in the diameter but even more pronounced in the depth. 367
 Though Fig. 16.10a presents a 3D reconstruction of all the 250 slices, more details 368
 can be observed when looking at the individual slices of Fig. 16.10b–l. The diam- 369
 eter of the pits in the low index (110) oriented grain are 150 ± 10 nm, while the 370
 diameter in the (321) oriented grains is only slightly bigger with 170 ± 10 nm. The 371
 depth however is much more influenced by the differences of sputter yield depend- 372
 ing on the crystal orientation, and hence the (110) grain shows only 55 ± 5 nm depth 373
 in contrast to the 200 ± 20 nm depth of the (321) grain, nearly a factor of 4 374
 between them. 375

376 **16.11 Prototyping: Samples Prepared for Cell Adhesion**
377 **Tests and Statistical Pattern Analysis**

378 After the initial tests for the feasibility of the patterning was finished successfully
379 on the batch of samples with small-scale pattern, the “real” prototyping on the
380 $400 \times 400 \mu\text{m}$ patterned areas had been started. As consensus between statistical
381 needs for ideally a high number of samples on one hand and the slow process of
382 patterning with the FIB on the other hand, five samples with each one area of
383 $120 \text{ nm pits}/240 \text{ nm pitch}$ and one area of $180 \text{ nm pits}/360 \text{ nm pitch}$ were
384 manufactured.

385 The two pit designs, A and B, were created on electropolished stainless steel
386 samples by FIB and are presented in Fig. 16.11. Three things can be observed. First,
387 the square areas that have been milled by the FIB are very different from the elec-
388 tropolished areas. Second, the triangular areas in the centre are much better defined
389 than the areas at the edges. Finally, within and outside these triangular areas, the
390 different colour tones observed are due to the polycrystallinity of the stainless steel
391 as described in detail in the previous section.

392 Alternatively, AFM was used to evaluate statistically in more depth the informa-
393 tion on topography, pit feature dimensions and as a comparison of the results
394 obtained via serial FIB–SEM sectioning. AFM examinations for this analysis were
395 performed in tapping mode using a Dimension 3100 with a Nanoscope IIIa control-
396 ler equipped with a phase imaging extender (Digital Instruments, Santa-Barbara,
397 CA, USA). The silicon cantilevers (purchased from Windsor Scientific, UK) have a
398 tip radius of less than 10 nm and a 40 N m^{-1} spring constant. AFM images were

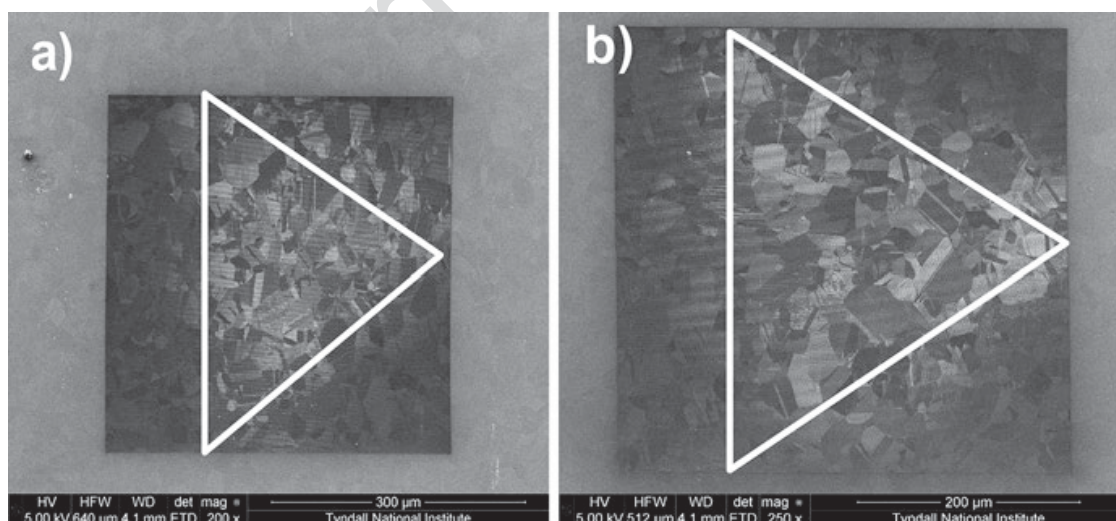


Fig. 16.11 Overview of SEM images of (a) design A and (b) design B showing (1) differences in milled (*inside the square area*) and electropolished surfaces (*outside the square area*), (2) *triangular areas* covering more than half of the $400 \mu\text{m} \times 400 \mu\text{m}$ *square* are much better defined than the areas at the corners in the *squares* and (3) different colour tones illustrate the polycrystallinity of the stainless steel

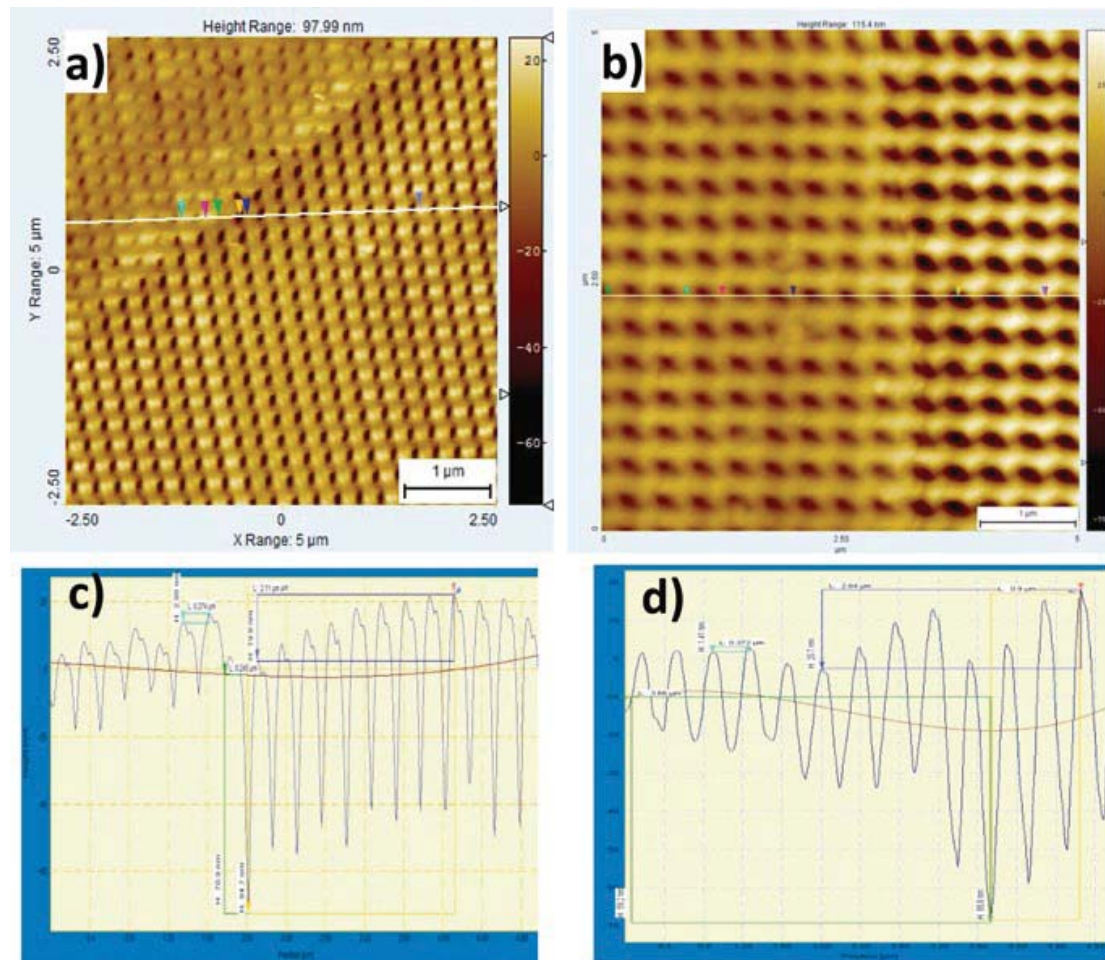


Fig. 16.12 AFM top view and cross-sectional images of pits (a, c) design A and (b, d) design B. Variation in depth dimensions from AFM profiles in region I and II is clearly noticed

recorded at a scan rate of 0.5 Hz and a resonance frequency of 300 kHz. Each 399
 sample was evaluated over scan fields of $5 \times 5 \mu\text{m}^2$, $1 \times 1 \mu\text{m}^2$ and $500 \times 500 \text{nm}^2$. 400
 The pit dimensions of the resulting images were evaluated using scanning probe 401
 imaging processor software (version 5.1.5). 402

Four nano-structured samples were used for the measurements. Four topographic 403
 measurements were performed in different random fields per substrate. Figure 16.12 404
 shows the 2D AFM images and profiles of designs A and B on $5 \times 5 \mu\text{m}^2$ areas. 405
 A similar trend was noticed with AFM data. Region I showed shallower structures 406
 than region II, Fig. 16.12a, b. From the AFM profiles across a $5 \mu\text{m}$ width as depicted 407
 in Fig. 16.12c, d, the average depth recorded in region I for design A and design B 408
 was $24 \pm 18 \text{ nm}$ and $26 \pm 20 \text{ nm}$ ($N=115$), whereas in region II the average depth 409
 was $68 \pm 48 \text{ nm}$ and $64 \pm 8.5 \text{ nm}$ ($N=115$). This variation of more than four times 410
 indicates that an exact match of the desired depth of 50–100 nm can only be 411
 approximated. 412

The images presented in Fig. 16.13a, b are of a closer SEM inspection of 413
 designs A and B on triangular areas of $5 \times 5 \mu\text{m}^2$. The pit structures within the 414
 triangular zones are circular as wanted for pit designs A and B (Fig. 16.13a, b). 415

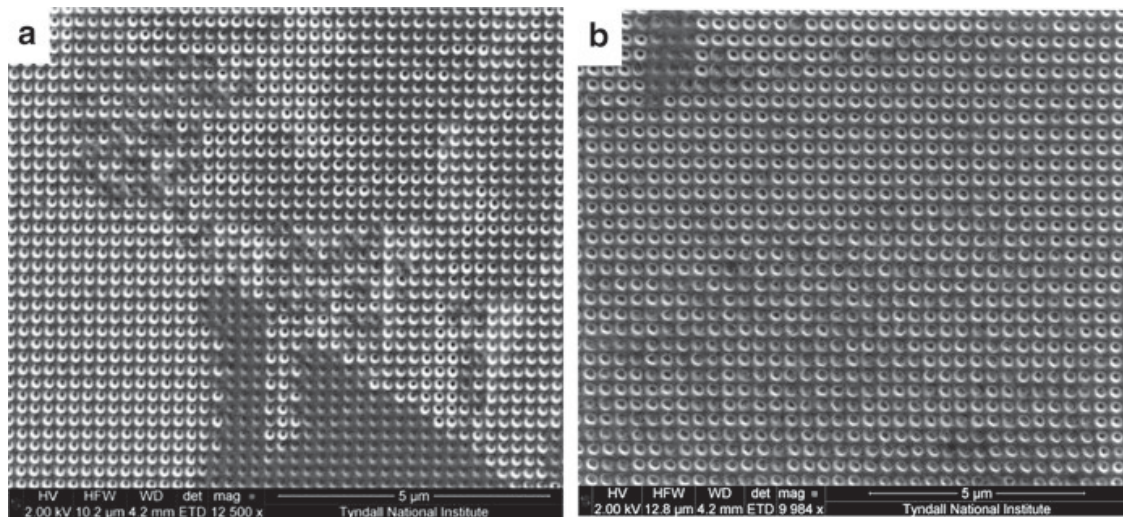


Fig. 16.13 SEM images of circular pits of (a and b) design A and B reproduced within the triangular areas

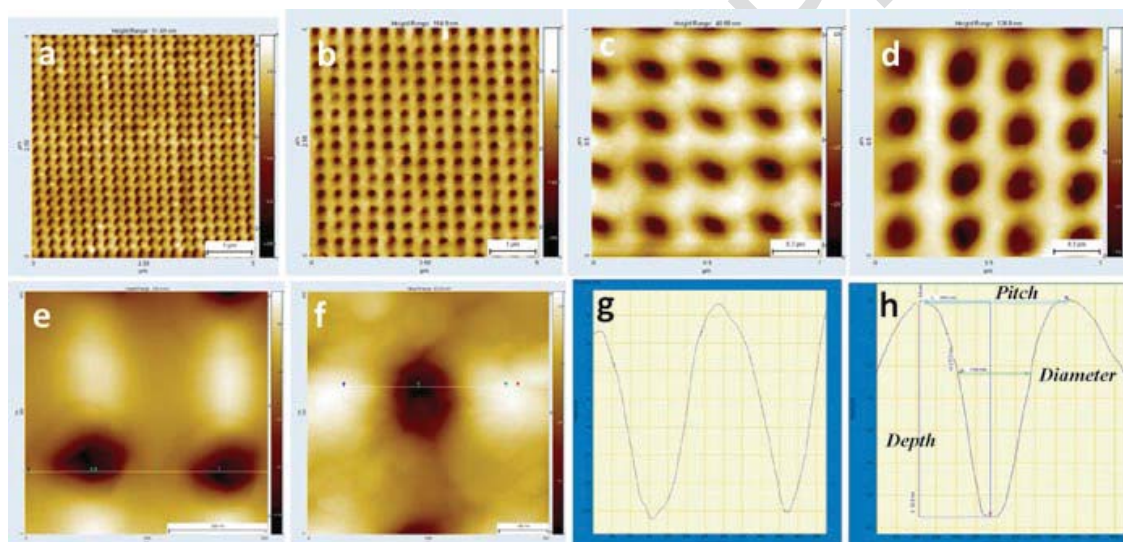


Fig. 16.14 AFM topographies of uniformly fabricated structures of (a, c, e) pits design A and (b, d, f) design B pits reproduced within the triangular areas (scale: $5 \times 5 \mu\text{m}$, $1 \times 1 \mu\text{m}$ and $500 \times 500 \text{ nm}$). Panels (g) and (h) represent the AFM profiles of (e) and (f) across the length of 500 nm

416 Smaller areas of about $150 \times 150 \mu\text{m}^2$ showed circular shapes when imaged in top-
 417 down direction in the whole patterned area in the preliminary tests.

418 However, from the AFM images the shapes of the pits in design A in triangular
 419 areas are more elliptical (Fig. 16.14a, c, e), whereas those of design B are closer to
 420 perfect holes (Fig. 16.14b, d, f). The pit structures for designs A and B outside the
 421 triangular areas exhibited deformed circular shapes as demonstrated in Fig. 16.15a, b.
 422 From the stigmated nature one can conclude that there are problems with the focus-
 423 ing and astigmatism caused by the FIB optics. This is not surprising as the 200 times
 424 magnification is close to the lower limit of the FIB Helios column.

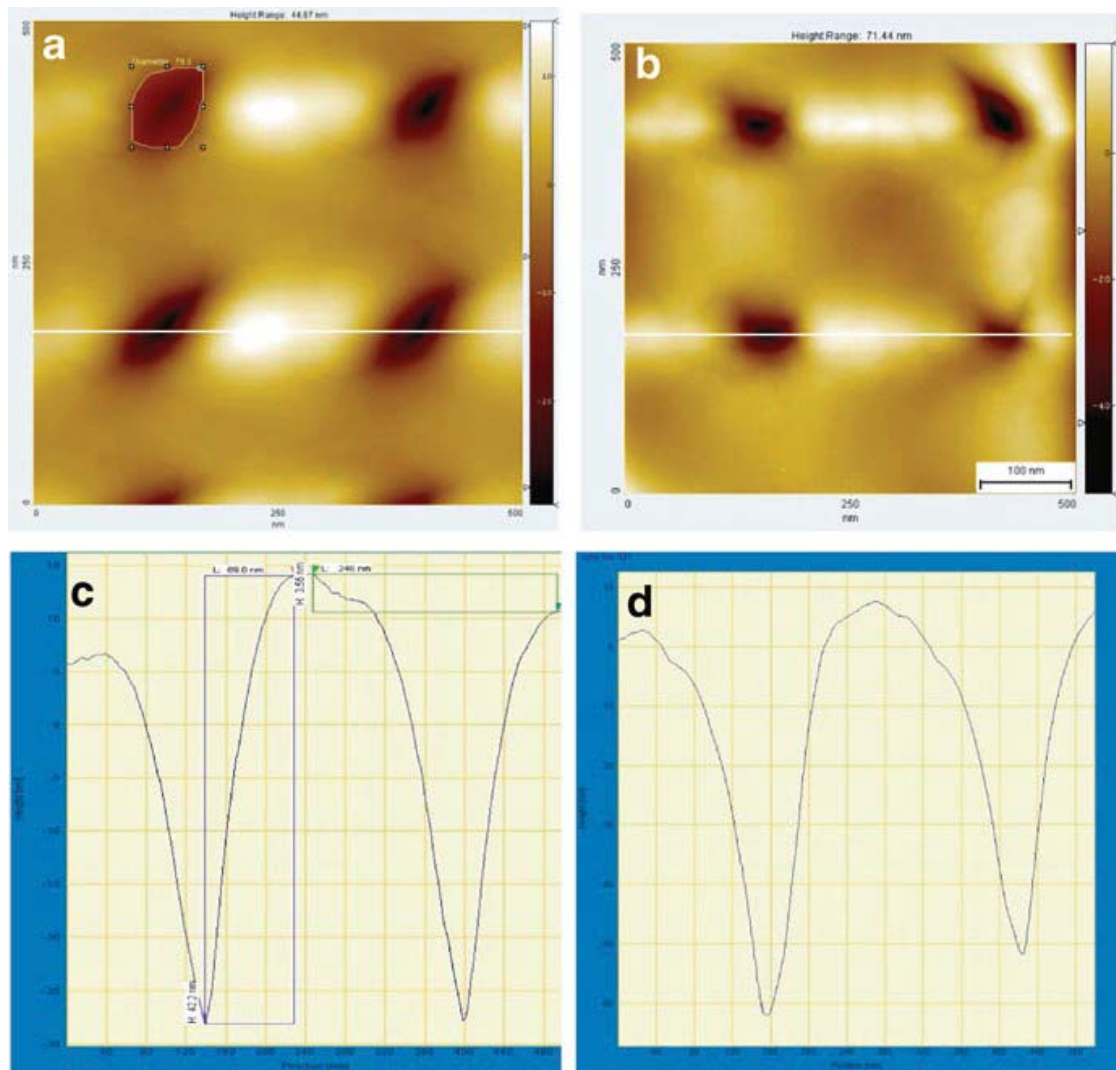


Fig. 16.15 AFM pictures of unevenly patterned pit structures of (a and b) designs A and design B reproduced outside the triangular areas (scale: 500×500 nm) and (c and d) profiles of (a) and (b) across the length of 500 nm

From the AFM profiles, the uniformity and distribution of the pits A and B parameters (or dimensions) such as diameter, depth and pitch produced by FIB technique were evaluated. The A and B pit dimensions were measured using a Nanoscope imaging probe software as described above.

The distribution curves of A and B pit dimensions were plotted and presented in Fig. 16.16. Figure 16.16a shows that when seeking to produce design A diameter pits ($N=162$), the result was far from uniform. Although the highest number of pits did fall within the 116–120 nm range, the graph shows there were considerable variations in resulting pit sizes.

In seeking to produce design B diameter pits ($N=90$), Fig. 16.16b shows a similar pattern to the result shown in the previous graph. The highest number of pits was between 181 and 185 nm range with the lowest amount of pits registering in the ranges above 180 nm.

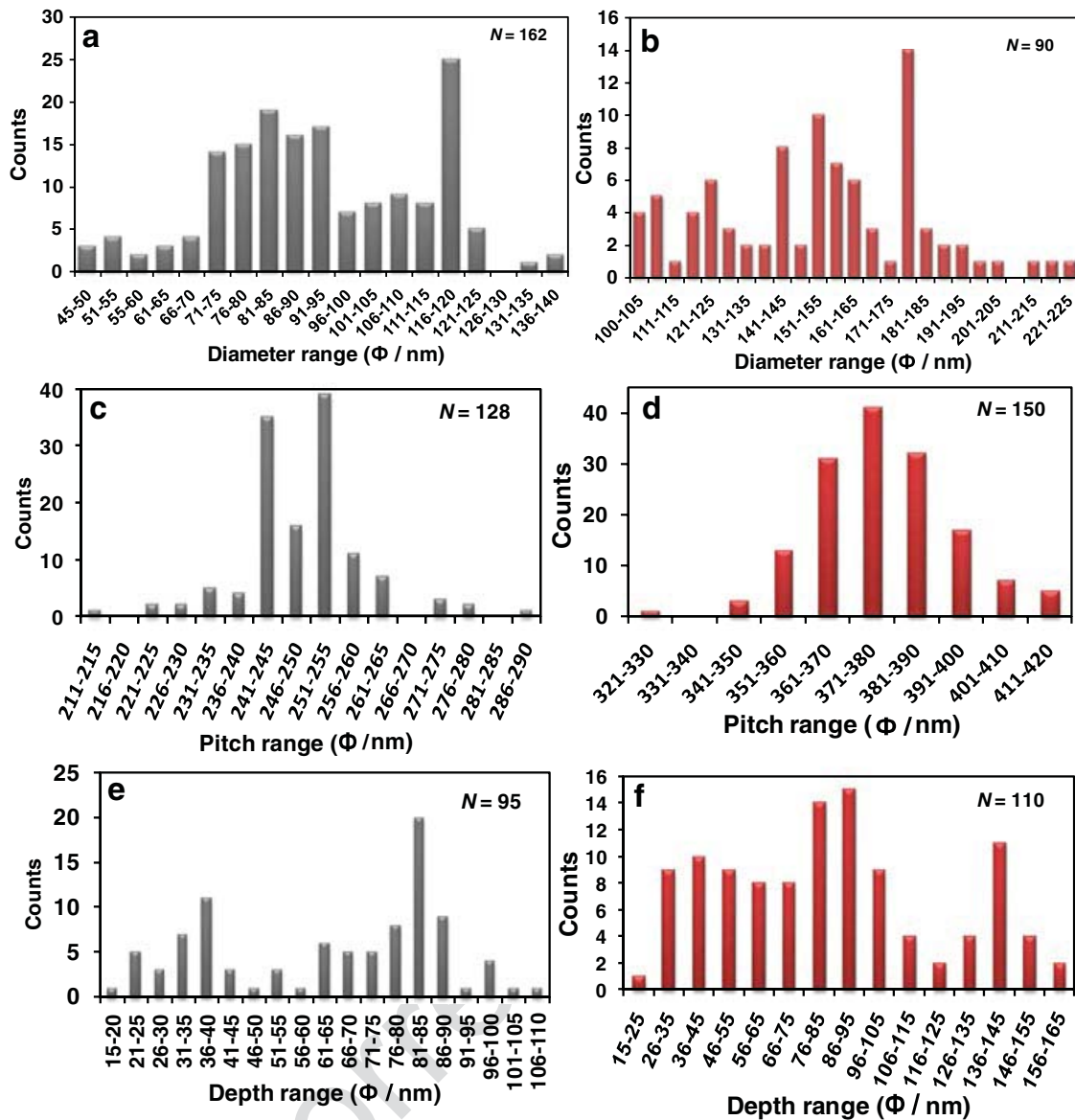


Fig. 16.16 Distribution curves of pit diameter of (a) and (b) 120 and 180 nm with a pitch of (c) and (d) 240 and 360 nm and depth of (e) and (f) 50–100 nm

438 The required A pitch range here (Fig. 16.16c) was 240 nm ($N=128$). Most pits
 439 registered between 251–255 and 241–245 nm then at 246–250 nm range. However,
 440 only four pits were reported at 240 nm.

441 In looking for a design B pitch level of 360 nm ($N=150$ nm) presented in
 442 Fig. 16.16d, only 13 pits fell within this range. The majority of pits registered at
 443 pitches higher than the required level of 360 nm, falling between 371 and 380 nm,
 444 and one pit range as high as 411–420 nm.

445 In searching for a design A depth of 50 or 100 nm ($N=95$), Fig. 16.16e shows
 446 that one pit reported at 46–50 nm range and four pits reported at 96–105 nm range.
 447 However, considerable variation is still noted in the dimensions of all pits.

448 Again looking for a design B depth of 50 or 100 nm ($N=110$), nine pits were
 449 recorded within the 46–55 nm range (Fig. 16.16f). Nine were found to have a depth

t2.1 **Table 16.2** Dimensions of 120 nm pits obtained with FIB patterning

t2.2	t2.3			Lowest	Highest
	Dimensions	Sites number	Mean ± SD (nm)	dimension value (nm)	dimension value (nm)
t2.4	Diameter	$N=162$	97 ± 8.5	46	138
t2.5	Pitch	$N=128$	250 ± 11	213	290
t2.6	Depth	$N=95$	65 ± 24	19	116

t3.1 **Table 16.3** Dimensions of 180 nm pits obtained with FIB patterning

t3.2	t3.3			Lowest	Highest
	Dimensions	Sites number	Mean ± SD (nm)	dimension value (nm)	dimension value (nm)
t3.4	Diameter	$N=90$	155 ± 11	10	221
t3.5	Pitch	$N=150$	375 ± 14	323	411
t3.6	Depth	$N=110$	84 ± 36	15	165

in the 96–105 nm range. However, some pits were also recorded above the desired 100 nm range which should have minor influence as long as they are deep enough to influence the cell adhesion.

The variations in pit dimensions demonstrated that FIB milling rate is greatly influenced by the polycrystalline structure of stainless steel and beam quality.

Tables 16.2 and 16.3 summarise the obtained pit dimensions of design A and B diameter ($N=162$ and 90 ; scan area, $1 \times 1 \mu\text{m}^2$) and pitch and depth ($N=128$ and 150 and 95 and 90 ; scan area, $5 \times 5 \mu\text{m}^2$) created by FIB milling. For the required 120 nm pit, the average pit had a diameter of 97 ± 8.5 nm ($N=162$), pitch of 250 ± 11 nm ($N=128$) and depth of 65 ± 24 nm ($N=95$), whereas for the 180 nm pit, the average pit had a diameter of 155 ± 11 nm ($N=90$), pitch of 375 ± 14 nm ($N=150$) and depth of 84 ± 36 nm ($N=110$).

Nevertheless, correlation of FIB–SEM and AFM cross-sectional imaging with the top-down appearance of known patterned area (grain) was essential in establishing accurate size and shape distribution of the formed pit structures.

All these variations in pit dimensions reported in stainless steel samples can be due to the atomic arrangement or random orientation of crystallographic structures and nonuniformity in grain size, though the shape of the incident beam at the point of impact on the sample surface will have the greatest effect of all the factors, followed by the crystallographic orientation of the grain at the surface.

16.12 In Vitro Cell Studies: Endothelial Cell Adhesion Tests 470

Finally, in vitro human EC culture and EC adhesion and densities studies were performed on unpolished, electropolished and nano-textured stainless steel surfaces.

Figure 16.17 shows the fluorescence images of the EC adhesion and densities after 1–5 days on unpolished, electropolished and design A and B surfaces. Very little significant difference in EC adhesion between these surfaces is revealed.

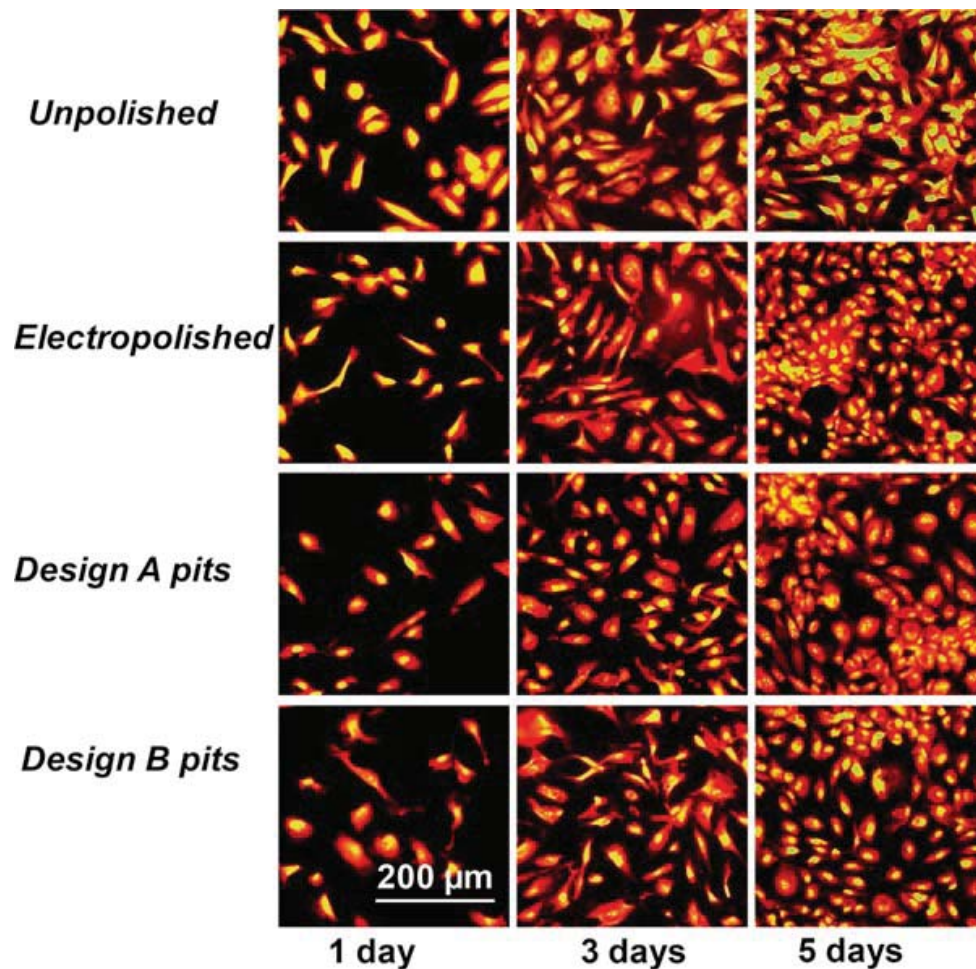


Fig. 16.17 Fluorescent images of EC cultured on (a) unpolished (b) electropolished, (c) design A pits and (d) design B pits on stainless steel surfaces after 1, 3 and 5 days

476 However, the morphology of ECs appears to be greatly defined on pits design A and
 477 B relative to electropolished and unpolished samples. After 1 day, EC densities
 478 were significantly lower on nano-structured 316L steel substrates when compared
 479 to unpolished and electropolished control samples. EC adhesion density was signifi-
 480 cantly greater after 5 days compared to 1 day for all substrates tested.

481 To confirm the significant difference in EC adhesion and densities after 1–5 days
 482 involving these surfaces as demonstrated by fluorescence data, EC counts were
 483 performed on each three substrate of interest ($N=12$).

484 16.13 Conclusion

485 FIB has compelling advantages for flexible prototyping compared to other tradi-
 486 tional techniques; however, the milling rates and the corresponding shape and size
 487 of the formed structures are largely affected by the grain size of the polycrystalline

316L stainless steel and stability of the ion beam quality over large areas. Moreover 488
 this method is practically limited to 120 nm resolution for the desired pit depth and 489
 uniform scan size of 200 $\mu\text{m} \times 200 \mu\text{m}$. Nevertheless formed structures show large 490
 variation of pit depths and shapes and as such surfaces might serve as a resourceful 491
 platform for screening large variations of cell/pattern stainless steel interactions. 492
 However, the FIB nano-pits design A and B created on polycrystalline stainless 493
 steel surfaces demonstrated low EC adhesion and proliferation relative to unpol- 494
 ished and electropolished specimens. There was no significant difference in EC 495
 adhesion and proliferation between unpolished–electropolished samples and design 496
 A and B pits. Further morphological examination of EC response on nano-structured 497
 steel surfaces would verify the mechanism for low EC adhesion and proliferation on 498
 these surfaces. Nano-patterning the stainless steel surfaces by FIB is time consum- 499
 ing and expensive, especially when patterning large areas. The precision and repro- 500
 ducibility of this technique is greatly affected by the polycrystallinity of stainless 501
 steel and a stable beam quality over large sample areas. 502

Acknowledgements This work was supported through a Starting Investigator Research Grant 503
 (09/SIRG/I1621) of the Science Foundation Ireland (SFI), the National Biophotonics and Imaging 504
 Platform, Ireland (NBIPI) and the Integrated NanoScience Platform for Ireland (INSPIRE) initia- 505
 tives funded by the Irish Government’s Programme for Research in Third Level Institutions, Cycle 506
 4, National Development Plan 2007–2013. The authors are grateful to Dr Shanthi Muttukrishna 507
 (Department of Obstetrics and Gynaecology, University College Cork) for the gift of the human 508
 umbilical vein endothelial vein. Dr Lynette Keeney is gratefully acknowledged for performance of 509
 the AFM scans and line profiles for the correlative microscopy part of this chapter. Dr Calum 510
 Dickinson is gratefully acknowledged for contributing the EBSD measurements. 511

References 512

1. Dugdale, D.C.: Stent, in *Medicine Plus*, 2012. <http://www.nlm.nih.gov/medlineplus/ency/article/002303.htm> 513
514
2. Balamurugan, A., Rajeswari, S., Balossier, G., Rebelo, A.H.S., Ferreira, J.M.F.: Corrosion 515
 aspects of metallic implants—an overview. *Mater. Corrosion* **59**(11), 855–869 (2008) 516
3. O’Brien, B., Carroll, W.: The evolution of cardiovascular stent materials and surfaces in 517
 response to clinical drivers: a review. *Acta Biomater.* **5**(4), 945–958 (2009) 518
4. Clerc, C.O., Jedwab, M.R., Mayer, D.W., Thompson, P.J., Stinson, J.S.: Assessment of 519
 wrought ASTM F1058 cobalt alloy properties for permanent surgical implants. *J. Biomed.* 520
Mater. Res. **38**(3), 229–234 (1997) 521
5. Craig, C., Friend, C., Edwards, M., Cornish, L., Gokcen, N.: Mechanical properties and micro- 522
 structure of platinum enhanced radiopaque stainless steel (PERSS) alloys. *J. Alloys Compd.* 523
361(1), 187–199 (2003) 524
6. Craig, C., Friend, C., Edwards, M., Gokcen, N.: Tailoring radiopacity of austenitic stainless 525
 steel for coronary stents. In: *Medical Device Materials: Proceedings from the Materials &* 526
Processes for Medical Devices Conference 2003, 8–10 September 2003, Anaheim, California. 527
 2004. American Society for Metals 528
7. Heublein, B., Rohde, R., Kaese, V., Niemeyer, M., Hartung, W., Haverich, A.: Biocorrosion of 529
 magnesium alloys: a new principle in cardiovascular implant technology? *Heart* **89**(6), 651– 530
 656 (2003) 531

- 532 8. Lüscher, T.F., Steffel, J., Eberli, F.R., Joner, M., Nakazawa, G., Tanner, F.C., Virmani, R.:
533 Drug-eluting stent and coronary thrombosis biological mechanisms and clinical implications.
534 *Circulation* **115**(8), 1051–1058 (2007)
- 535 9. Daemen, J., Wenaweser, P., Tsuchida, K., Abrecht, L., Vaina, S., Morger, C., Kukreja, N., Jüni,
536 P., Sianos, G., Hellige, G.: Early and late coronary stent thrombosis of sirolimus-eluting and
537 paclitaxel-eluting stents in routine clinical practice: data from a large two-institutional cohort
538 study. *Lancet* **369**(9562), 667–678 (2007)
- 539 10. Chou, L., Firth, J.D., Uitto, V.-J., Brunette, D.M.: Substratum surface topography alters cell
540 shape and regulates fibronectin mRNA level, mRNA stability, secretion and assembly in
541 human fibroblasts. *J. Cell Sci.* **108**(4), 1563–1573 (1995)
- 542 11. Boyan, B.D., Hummert, T.W., Dean, D.D., Schwartz, Z.: Role of material surfaces in regulat-
543 ing bone and cartilage cell response. *Biomaterials* **17**(2), 137–146 (1996)
- 544 12. Craighead, H.G., James, C.D., Turner, A.M.P.: Chemical and topographical patterning for
545 directed cell attachment. *Curr. Opin. Solid State Mater. Sci.* **5**(2–3), 177–184 (2001)
- 546 13. Curtis, A., Wilkinson, C.: Nanotechniques and approaches in biotechnology. *Trends*
547 *Biotechnol.* **19**(3), 97–101 (2001)
- 548 14. Kogler, P., Clayton, A., Thissen, H., Santos, G.N.C., Kingshott, P.: The influence of nano-
549 structured materials on biointerfacial interactions. *Adv. Drug Deliv. Rev.* **64**(15), 1820–1839
550 (2012)
- 551 15. Nikkhah, M., Edalat, F., Manoucheri, S., Khademhosseini, A.: Engineering microscale topog-
552 raphies to control the cell–substrate interface. *Biomaterials* **33**(21), 5230–5246 (2012)
- 553 16. Chen, L., Han, D., Jiang, L.: On improving blood compatibility: from bioinspired to synthetic
554 design and fabrication of biointerfacial topography at micro/nano scales. *Colloids Surf. B*
555 *Biointerfaces* **85**(1), 2–7 (2011)
- 556 17. Gentile, F., Tirinato, L., Battista, E., Causa, F., Liberale, C., di Fabrizio, E.M., Decuzzi, P.:
557 Cells preferentially grow on rough substrates. *Biomaterials* **31**(28), 7205–7212 (2010)
- 558 18. Kasemo, B.: Biological surface science. *Surf. Sci.* **500**(1–3), 656–677 (2002)
- 559 19. Duncan, A.C., Weisbuch, F., Rouais, F., Lazare, S., Baquey, C.: Laser microfabricated model
560 surfaces for controlled cell growth. *Biosens. Bioelectron.* **17**(5), 413–426 (2002)
- 561 20. Berry, C.C., Campbell, G., Spadiccino, A., Robertson, M., Curtis, A.S.G.: The influence of
562 microscale topography on fibroblast attachment and motility. *Biomaterials* **25**(26), 5781–5788
563 (2004)
- 564 21. Yim, E.K.F., Leong, K.W.: Significance of synthetic nanostructures in dictating cellular
565 response. *Nanomedicine* **1**(1), 10–21 (2005)
- 566 22. Falconnet, D., Csucs, G., Grandin, H.M., Textor, T.: Surface engineering approaches to
567 micropattern surfaces for cell-based assays. *Biomaterials* **27**(16), 3044–3063 (2006)
- 568 23. Yu, L.M.Y., Leipzig, N.D., Shoichet, M.S.: Promoting neuron adhesion and growth. *Mater.*
569 *Today* **11**(5), 36–43 (2008)
- 570 24. Roach, P., Parker, T., Gadegaard, N., Alexander, M.R.: Surface strategies for control of neuro-
571 nal cell adhesion: a review. *Surf. Sci. Rep.* **65**(6), 145–173 (2010)
- 572 25. Nazneen, F., Herzog, G., Arrigan, D.W., Caplice, N., Benvenuto, P., Galvin, P., Thompson, M.:
573 Surface chemical and physical modification in stent technology for the treatment of coronary
574 artery disease. *J. Biomed. Mater. Res. B Appl. Biomater.* **100**, 1989–2014 (2012)
- 575 26. Norman, J.J., Desai, T.A.: Methods for fabrication of nanoscale topography for tissue engi-
576 neering scaffolds. *Ann. Biomed. Eng.* **34**(1), 89–101 (2006)
- 577 27. Buzea, C., Beydaghyan, G., Elliott, C., Robbie, K.: Control of power law scaling in the growth
578 of silicon nanocolumn pseudo-regular arrays deposited by glancing angle deposition.
579 *Nanotechnology* **16**(10), 1986 (2005)
- 580 28. Dolatshahi-Pirouz, A., Hovgaard, M.B., Rechendorff, K., Chevallier, J., Foss, M., Besenbacher,
581 F.: Scaling behavior of the surface roughness of platinum films grown by oblique angle deposi-
582 tion. *Phys. Rev. B* **77**(11), 115427 (2008)
- 583 29. Tseng, A.A., Notargiacomo, A.: Nanoscale fabrication by nonconventional approaches.
584 *J. Nanosci. Nanotechnol.* **5**(5), 683–702 (2005)

30. Sarkar, S., Dadhania, M., Rourke, P., Desai, T.A., Wong, J.Y.: Vascular tissue engineering: microtextured scaffold templates to control organization of vascular smooth muscle cells and extracellular matrix. *Acta Biomater.* **1**(1), 93–100 (2005) 585
586
587
31. Houtchens, G.R., Foster, M.D., Desai, T.A., Morgan, E.F., Wong, J.Y.: Combined effects of microtopography and cyclic strain on vascular smooth muscle cell orientation. *J. Biomech.* **41**(4), 762–769 (2008) 588
589
590
32. Biela, S.A., Su, Y., Spatz, J.P., Kemkemer, R.: Different sensitivity of human endothelial cells, smooth muscle cells and fibroblasts to topography in the nano–micro range. *Acta Biomater.* **5**(7), 2460–2466 (2009) 591
592
593
33. Green, A.M., Jansen, J.A., Van der Waerden, J.P.C.M., Von Recum, A.F.: Fibroblast response to microtextured silicone surfaces: texture orientation into or out of the surface. *J. Biomed. Mater. Res.* **28**(5), 647–653 (1994) 594
595
596
34. Walboomers, X., Croes, H., Ginsel, L., Jansen, J.: Contact guidance of rat fibroblasts on various implant materials. *J. Biomed. Mater. Res.* **47**(2), 204–212 (1999) 597
598
35. Walboomers, X., Croes, H., Ginsel, L., Jansen, J.: Growth behavior of fibroblasts on microgrooved polystyrene. *Biomaterials* **19**(20), 1861–1868 (1998) 599
600
36. Walboomers, X., Ginsel, L., Jansen, J.: Early spreading events of fibroblasts on microgrooved substrates. *J. Biomed. Mater. Res.* **51**(3), 529–534 (2000) 601
602
37. Walboomers, X., Monaghan, W., Curtis, A., Jansen, J.: Attachment of fibroblasts on smooth and microgrooved polystyrene. *J. Biomed. Mater. Res.* **46**(2), 212–220 (1999) 603
604
38. Loesberg, W.A., te Riet, J., van Delft, F.C., Schön, P., Figdor, C.G., Speller, S., van Loon, J.J., Walboomers, X.F., Jansen, J.A.: The threshold at which substrate nanogroove dimensions may influence fibroblast alignment and adhesion. *Biomaterials* **28**(27), 3944–3951 (2007) 605
606
607
39. Dalby, M.J., Gadegaard, N., Riehle, M.O., Wilkinson, C.D.W., Curtis, A.S.G.: Investigating filopodia sensing using arrays of defined nano-pits down to 35 nm diameter in size. *Int. J. Biochem. Cell Biol.* **36**(10), 2005–2015 (2004) 608
609
610
40. Dalby, M.J., Gadegaard, N., Wilkinson, C.D.: The response of fibroblasts to hexagonal nanotopography fabricated by electron beam lithography. *J. Biomed. Mater. Res. A* **84**(4), 973–979 (2008) 611
612
613
41. Yim, E.K.F., Reano, R.M., Pang, S.W., Yee, A.F., Chen, C.S., Leong, K.W.: Nanopattern-induced changes in morphology and motility of smooth muscle cells. *Biomaterials* **26**(26), 5405–5413 (2005) 614
615
616
42. Lee, S.W., Kim, S.Y., Rhyu, I.C., Chung, W.Y., Leesungbok, R., Lee, K.W.: Influence of microgroove dimension on cell behavior of human gingival fibroblasts cultured on titanium substrata. *Clin. Oral Implants Res.* **20**(1), 56–66 (2009) 617
618
619
43. Ito, T., Okazaki, S.: Pushing the limits of lithography. *Nature* **406**(6799), 1027–1031 (2000) 620
44. Chou, S.Y., Krauss, P.R., Renstrom, P.J.: Imprint of sub-25 nm vias and trenches in polymers. *Appl. Phys. Lett.* **67**(21), 3114–3116 (1995) 621
622
45. Raffa, V., Castrataro, P., Menciassi, A., Dario, P.: Focused Ion Beam as a Scanning Probe: Methods and Applications. *Applied Scanning Probe Methods II*, pp. 361–412. Springer, New York, NY (2006) 623
624
625
46. Iordanova, I., Antonov, V., Gurkovsky, S.: Changes of microstructure and mechanical properties of cold-rolled low carbon steel due to its surface treatment by Nd:glass pulsed laser. *Surf. Coat. Technol.* **153**(2–3), 267–275 (2002) 626
627
628
47. Duncan, A.C., Rouais, F., Lazare, S., Bordenave, L., Baquey, C.: Effect of laser modified surface microtopochemistry on endothelial cell growth. *Colloids Surf. B Biointerfaces* **54**(2), 150–159 (2007) 629
630
631
48. Kalantar-Zadeh, K., Fry, B.: *Nanotechnology Enabled Sensors*. Springer, New York, NY (2007) 632
49. Volkert, C., Minor, A.: Focused ion beam microscopy and micromachining. *MRS Bull.* **32**(5), 389–395 (2007) 633
634
50. Lanyon, Y.H., De Marzi, G., Watson, Y.E., Quinn, A.J., Gleeson, J.P., Redmond, G., Arrigan, D.W.: Fabrication of nanopore array electrodes by focused ion beam milling. *Anal. Chem.* **79**(8), 3048–3055 (2007) 635
636
637

- 638 51. Choi, C.H., Heydarkhan-Hagvall, S., Wu, B.M., Dunn, J.C., Beygui, R.E., Kim, C.J.: Cell
639 growth as a sheet on three-dimensional sharp-tip nanostructures. *J. Biomed. Mater. Res.*
640 *A* **89**(3), 804–817 (2009)
- 641 52. Raffa, V., Vittorio, O., Pensabene, V., Menciassi, A., Dario, P.: FIB-nanostructured surfaces
642 and investigation of bio/nonbio interactions at the nanoscale. *IEEE Trans. NanoBiosci.* **7**(1),
643 1–10 (2008)
- 644 53. Joshi, K., Singh, P., Verma, S.: Fabrication of platinum nanopillars on peptide-based soft struc-
645 tures using a focused ion beam. *Biofabrication* **1**(2), 025002 (2009)
- 646 54. Choubey, A., Marton, D., Sprague, E.A.: Human aortic endothelial cell response to 316L stain-
647 less steel material microstructure. *J. Mater. Sci. Mater. Med.* **20**(10), 2105–2116 (2009)
- 648 55. Misra, R.D., Nune, C., Pesacreta, T.C., Somani, M.C., Karjalainen, L.P.: Understanding the
649 impact of grain structure in austenitic stainless steel from a nanograined regime to a coarse-
650 grained regime on osteoblast functions using a novel metal deformation–annealing sequence.
651 *Acta Biomater.* **9**, 6245–6258 (2013)
- 652 56. Russell, A., Lee, K.L.: *Structure-Property Relations in Nonferrous Metals*. Wiley-Interscience,
653 New York, NY (2005)
- 654 57. Shi, D.: *Introduction to Biomaterials*. World Scientific, London (2006)
- 655 58. Nazneen, F., Galvin, P., Arrigan, D.W., Thompson, M., Benvenuto, P., Herzog, G.:
656 Electropolishing of medical-grade stainless steel in preparation for surface nano-texturing.
657 *J. Solid State Electrochem.* **16**(4), 1389–1397 (2012)
- 658 59. Dalby, M.J., Berry, C.C., Riehle, M.O., Sutherland, D.S., Agheli, H., Curtis, A.S.G.: Attempted
659 endocytosis of nano-environment produced by colloidal lithography by human fibroblasts.
660 *Exp. Cell Res.* **295**(2), 387–394 (2004)
- 661 60. Schmidt, M., Nazneen, F., Georgiev, Y., Herzog, G., Galvin, P., Petkov, N.: FIB patterning of
662 stainless steel for the development of nano-structured stent surfaces for cardiovascular applica-
663 tions. *J. Phys. Conf.* **371**(1), 012065 (2012)
- 664 61. Nazneen, F., Schmidt, M., McLoughlin, E., Petkov, N., Herzog, G., Arrigan, D., Galvin, P.: [AU4]
665 Nano-texturing of medical-grade 316L stainless steel by focused ion beam for endothelial cell
666 studies. *J. Nanosci. Nanotechnol.*, 2013.
- 667 62. Feitknecht, W.: Über den angriff von krystallen durch kanalstrahlen. *Helv. Chim. Acta* **7**(1),
668 825–842 (1924)
- 669 63. Wehner, G.K.: Controlled sputtering of metals by low-energy Hg ions. *Phys. Rev.* **102**(3),
670 690–704 (1956)
- 671 64. Wehner, G.K., Rosenberg, D.: Angular distribution of sputtered material. *J. Appl. Phys.* **31**(1),
672 177–179 (1960)
- 673 65. Sigmund, P.: Theory of sputtering. I. Sputtering yield of amorphous and polycrystalline tar-
674 gets. *Phys. Rev.* **184**(2), 383–416 (1969)
- 675 66. Bean, K.E.: Anisotropic etching of silicon. *IEEE Trans. Electron Dev.* **25**(10), 1185–1193
676 (1978)
- 677 67. Seidel, H., Csepregi, L., Heuberger, A., Baumgärtel, H.: Anisotropic etching of crystalline sili-
678 con in alkaline solutions I. Orientation dependence and behavior of passivation layers.
679 *J. Electrochem. Soc.* **137**(11), 3612–3626 (1990)
- 680 68. Schmidt, M., Nazneen, F., Herzog, G., Arrigan, D., Galvin, P., Keeney, L., Petkov, N., Holmes, [AU5]
681 J.D.: to be submitted.
- 682 69. Schmidt, M., Nazneen, F., Herzog, G., Arrigan, D., Galvin, P., Dickinson, C., de Silva, J.P., [AU6]
683 Scanlan, D., O'Hara, N., Cross, G.L.W.: Correlative microscopy study of FIB patterned stain-
684 less steel surfaces as novel nano-structured stents for cardiovascular applications. *MRS Proc*
685 *2012*. 1466(1).
- 686 70. Giannuzzi, L., Stevie, F.: A review of focused ion beam milling techniques for TEM specimen
687 preparation. *Micron* **30**(3), 197–204 (1999)
- 688 71. Schwartz, A.J., Kumar, M., Adams, B.L., Field, D.P.: *Electron Backscatter Diffraction in*
689 *Materials Science*. Springer, New York, NY (2009)
- 690 72. Stark, Y., Fromter, R., Stickler, D., Oepen, H.P.: Sputter yields of single- and polycrystalline metals
691 for application in focused ion beam technology. *J. Appl. Phys.* **105**(1), 013542-1–013542-5 (2009)